A Rigorous Solution to the Problem of Phase Behavior in Unconventional Formations With High Capillary Pressure

Sajjad S. Neshat, Ryosuke Okuno, and **Gary A. Pope,** University of Texas at Austin

Summary

Phase behavior of hydrocarbon mixtures is affected by the petrophysical properties of the formation. This paper integrates several important thermodynamic and petrophysical aspects of the problem in a rigorous way and introduces a solution that can be applied over the range of pore sizes in tight and shale formations in which hydrocarbons can be practically recovered. A new criterion for phase-stability analysis is introduced that results in discovery of a new range of solutions for the capillary equilibrium problem. A novel three-phase capillary pressure model has been used to estimate the effect of connate water on the gas/oil capillary pressure. The model is then used in conjunction with the new stability method to solve several phase-behavior problems for binary and multicomponent reservoir fluids. We show that the new approach can significantly improve the estimation of phase behavior at high capillary pressure.

Introduction

Thermodynamic behavior of reservoir fluids in unconventional formations has attracted much attention in recent years because of the soaring importance of such resources in the global energy supply. In shale and tight reservoirs, hydrocarbon mixtures manifest an altered behavior that potentially affects oil and gas production. This is primarily attributed to the existence of very small pores where capillary pressure, confinement, and adsorption play a role. Several authors have investigated the effect of each parameter under reservoir conditions. The reported experimental and theoretical studies suggest different—and to some extent contradictory—perspectives regarding the significance of these parameters. However, they all confirm that the pore size used in their calculations is the most-influential factor.

Nelson (2009) gathered and classified published data on pore-throat size of tight gas sandstone and shales in North America. Nelson (2009) reported that pore-throat diameters range from approximately 10 to 200 nm in tight gas sandstones and from 5 to 100 nm in shales. The average and median of all samples are greater than 12 nm, with small fractions of overall porosity in pore spaces smaller than 10 nm. Similar results were reported by Loucks et al. (2009), Clarkson et al. (2013), Al Hinai et al. (2014), Xu and Torres-Verdin (2014), Sigal (2015), and Zhang et al. (2017) for various unconventional reservoir rock samples around the globe. Newsham et al. (2004) and Dernaika et al. (2015), among many others, reported that the formations with average pore size smaller than 10 nm act as flow baffles, barriers, and seals. These observations indicate that pores smaller than 10 nm make an insignificant contribution to oil and gas recovery. Furthermore, connate water may occupy the smallest pores (Sigmund et al. 1973). For such cases, the hydrocarbon will occupy even larger pores. For pores larger than 10 nm, adsorption and confinement have negligible effects on fluid properties (Campos et al. 2009; Singh et al. 2009; Travalloni et al. 2010; Russo et al. 2011; Barsotti et al. 2016), so capillary pressure remains the only significant parameter.

Capillary pressure in porous media is a function of pore-size distribution, phase saturations, wettability, porosity, and permeability of the rock as well as fluid composition. In nanopores with a highly curved interface between the fluids, capillary pressure can exceed hundreds of psi and can affect the phase equilibrium. Many authors have used a single-tube model (STM) with an average pore radius to estimate the capillary pressure and evaluate its effect on the thermodynamic properties, such as bubblepoint and dewpoint pressures (Brusilovsky 1992; Nojabaei et al. 2013; Sandoval et al. 2016). An STM is not representative of heterogeneous formations with wide pore-size distributions, which leads to unreliable phase-behavior predictions. For example, the vaporization process starts from the largest-available pores in the rock and the condensation from the smallest pores (Sigmund et al. 1973). This implies that assuming a uniform radius results in overestimating bubblepoint suppression and also underestimating dewpoint increment in unconventional oil and condensate reservoirs. Wang et al. (2016) divided the porous medium into larger and smaller pores to partially account for the effect of pore-size distribution on bubblepoint and dewpoint pressures, although an STM was still used for each part.

Capillary pressure as a function of saturation of two phases has been measured for several tight and shale formations using different experimental methods (Newsham et al. 2004; Xu and Torres-Verdin 2014). However, it is known that the existence of a third phase can significantly affect the capillary pressure for each phase pair (Kalaydjian 1992; Bradford and Leij 1995; Virnovsky et al. 2004). This implies that existence of connate water affects the oil/gas capillary pressure and consequently the equilibrium phase behavior even if the solubility of water in the gas or oil is neglected. A general three-phase capillary pressure function is needed that accounts for the effect of all existing phase saturations (i.e., oil, gas, and water), as well as other relevant petrophysical properties of the rock such as wettability, pore structure, and pore-size distribution (Neshat and Pope 2017).

A necessary condition for equilibrium between two phases with a curved interface is that the chemical potential of each component evaluated at the pressure of each phase be the same in both phases. As capillary pressure increases, the wetting phase with lower pressure enters the metastable region and eventually reaches the spinodal point. The nonwetting phase at higher pressure also changes but remains in the stable region. Shapiro and Stenby (2001) showed that the boundary where capillary equilibrium is possible coincides with the spinodal point, and for capillary pressures greater than this limit, the equality of chemical potentials cannot be satisfied. Rezaveisi et al. (2015) solved this problem in compositional space for easier interpretation in compositional-simulation applications. By plotting the curves of hypothetical single-phase Gibbs free energy vs. mole fraction for a binary mixture, they showed that a capillary equilibrium solution with minimum Gibbs free energy is possible only if a common tangent line can be constructed between the

---

This paper (SPE 187260) was accepted for presentation at the SPE Annual Technical Conference and Exhibition, San Antonio, Texas, USA, 9–11 October 2017, and revised for publication. Original manuscript received for review 11 July 2017. Revised manuscript received for review 5 January 2018. Paper peer approved 22 January 2018.

two curves at different pressures. They assumed that the failure in finding a tangent line (or tangent plane for multicomponent mixtures) corresponds to having a single-phase solution, which leads to a discontinuity in the solution for higher values of capillary pressure. These authors also demonstrated that the tangent-plane-distance criterion for a stability test is not, in general, valid when capillary pressure is taken into account.

The effect of capillary pressure on the phase behavior of fluids in unconventional reservoirs has been investigated by several authors, but these studies have several problems that limit their practical use. In particular, there was a need for a reliable petrophysical model (i.e., capillary pressure), including the effect of all important features, including pore-size distribution and connate-water saturation. The choice of the equation of state (EOS) and its parameters—e.g., binary-interaction coefficients (BICs) and volume-shift parameters (VSPs)—and the correlation used for interfacial tension (IFT) may also affect the predicted phase behavior. Thus, a complete solution to the problem should incorporate the effects of all these parameters in a rigorous way.

In this study, we present a rigorous investigation into the problem of phase behavior at high capillary pressures. First, a general three-phase capillary pressure model is introduced and verified to calculate the oil/gas capillary pressure with connate water, and then it is calibrated for shale and tight formations using measured data. After that, the phase stability is discussed using the calibrated capillary pressure function. We suggest a new criterion for selection of the roots of a cubic EOS that enables solutions to be found at higher capillary pressure than previously possible. We show that with this method, the problem can be solved over the practical range of pore sizes in unconventional reservoirs using measured data from the literature. The new approach is then used for several pressure/volume/temperature calculations such as estimation of bubblepoint and dewpoint, constant-volume depletion (CVD), and constant-mass expansion (CME) for binary and multicomponent mixtures under reservoir conditions.

Oil/Gas Capillary Pressure in Presence of Connate Water

For a given geometry, capillary pressure between two phases depends on the curvature of the interface, contact angle, and IFT according to the Laplace equation. In a porous medium with pore-size distribution, the interface curvature is defined by pore-throat diameter estimated by saturation-dependent functions. In the presence of a third phase, the distribution of the phases in different pore sizes is affected depending on the wettability condition. For example, in water-wet reservoirs, connate water occupies the smallest pores and the oil/gas interface shifts to the larger pores. This important effect must be reflected precisely when capillary pressure is modeled.

Neshat and Pope (2017) developed coupled three-phase relative permeability and capillary pressure models that can be applied for all wettability conditions. The models include desirable features such as three-phase hysteresis and compositional consistency. In this study, we use a simplified version of the original model with a slight modification to calculate oil/gas capillary pressure in the presence of connate water and present an independent verification of this model using experimental data from the literature. The modified three-phase function is

$$P_{c,og} = \sigma_{og}\cos\theta_{og}\sqrt{\frac{\phi}{k}}\left[\frac{b_o}{(S_o+S_{wc})^{a_o}}+\frac{b_g}{(S_g)^{a_g}}\right], \quad \text{(1)}$$

where the saturations add up to unity. The parameters (b_o, b_g, a_o, a_g) depend on wettability and pore structure of the rock. Eq. 1 was used to fit the three-phase capillary pressure data reported by Kalaydjian (1992). **Fig. 1** shows good agreement between the model and data.

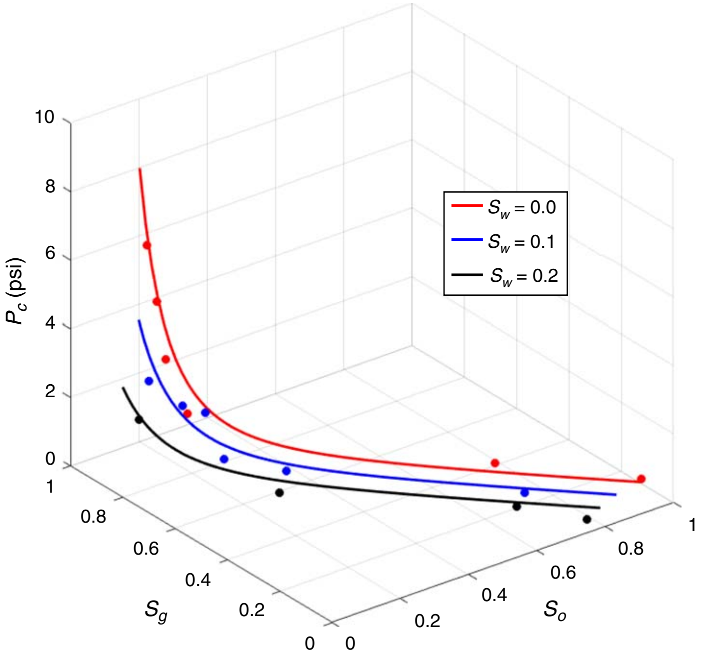

Fig. 1—Matching of three-phase oil/gas capillary pressure data at different connate-water saturations (blue and black curves) using the tuning parameters determined from two-phase measurements (red curve). Two- and three-phase experimental data are from Kalaydjian (1992). The fitting parameters and measured porosity and permeability (b_o, b_g, a_o, a_g, ϕ, k) are 4.3×10^{-4}, 0, 2.8, 2.2, 15%, and 480 md. σ_{og} = 27 dynes/cm.

Shale formations have wide and complex pore-size distributions—e.g., bimodal patterns (Kuila and Prasad 2013; Xu and Torres-Verdin 2014, Mehrabi et al. 2017). The two terms as expressed in Eq. 1 introduce enough flexibility into the model to capture the complexities of capillary pressure in unconventional reservoirs. **Fig. 2a** shows three pore-size distributions from different unconventional samples. Fig. 2b depicts the corresponding two-phase capillary pressure data matched by the model. The three-phase values can be predicted by changing S_{wc} in Eq. 1, although no three-phase capillary pressure data could be found to validate this approach for shales.

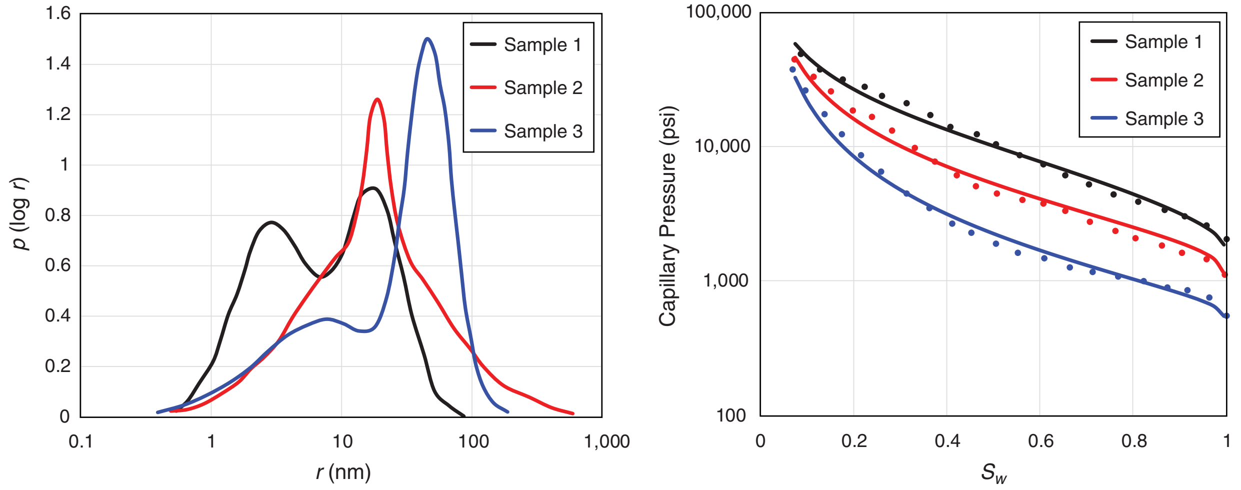

(a)

(b)

Fig. 2—(a) Pore-size distributions in three different unconventional samples; the *x*-axis is shown in log scale to better indicate the distribution patterns (Xu and Torres-Verdin 2014). (b) Air/mercury capillary pressure in the three samples as both measured (symbols) and calculated (solid lines) by Eq. 1 at zero connate-water saturation. The fitting parameters and measured porosity and permeability (b_o, b_g, a_o, a_g, ϕ, k) are 0.851, –0.709, 0.6, 0.01, 5%, and 8×10^{-4} md for Sample 1; 0.386, –0.193, 1.0, 0.06, 7%, and 4×10^{-3} md for Sample 2, and 0.100, –0.027, 1.35, 0.1, 4.5%, and 9×10^{-3} md for Sample 3. The IFT between air and mercury is 486 dynes/cm.

Equilibrium Calculations and Stability Analysis

After introducing the new capillary pressure model, the next step is to use this model in thermodynamic calculations. At equilibrium state in the presence of a curved interface, the following equations must be satisfied:

$$\mu_{io}(P_o,\vec{x}) = \mu_{ig}(P_g,\vec{y}), \quad (2)$$

$$P_g - P_o = P_c. \quad (3)$$

The chemical potentials are computed using either the Peng-Robinson (PR) (Peng and Robinson 1976) or Soave-Redlich-Kwong (SRK) (Soave 1972) EOSs. Eqs. 2 and 3 can be solved by either successive substitution (SS) or implicit methods. In the SS method, the Wilson correlation is used to obtain the initial guess. The first iteration is performed by solving the Rachford-Rice equation (Rachford and Rice 1952) with zero capillary pressure. The resulting phase compositions and compressibility factors are used to calculate IFT and saturations, which are then used to calculate the capillary pressure. The calculations are repeated until the convergence criterion is satisfied. At very low wetting-phase saturations, the capillary pressure function expressed by Eq. 1 becomes very steep. Thus, the capillary pressure undergoes a large change even with small variations in saturation during the iterations. To improve the convergence at low wetting-phase saturations, it is recommended to switch to an implicit method after a few SS iterations.

Identification of the reference phase in Eq. 3 should be performed using plausible physics. **Fig. 3** shows two examples of an isothermal-depletion process. The temperature in Process A is higher than the critical value, and the mixture exists as a single-phase gas at the initial condition. A liquid condensate exists at lower than the upper dewpoint pressure. As the pressure decreases, the condensate saturation increases to a maximum and then decreases until the mixture returns to the single-phase gas state at low pressure. During the retrograde process, gas is the continuous phase. The liquid pressure is calculated by subtracting capillary pressure from the gas pressure. In Process B, the temperature is lower than the critical temperature. Oil is the continuous phase and should be selected as the reference phase.

The equality of chemical potentials as expressed in Eq. 2 is a necessary but not-sufficient requirement for phase equilibrium. The Gibbs free energy must also be a minimum. For flash calculations without capillary pressure, the tangent-plane-distance method can be used to check the criterion of minimum Gibbs free energy (Michelsen 1982). Rezaveisi et al. (2015) realized that this approach is not always valid when capillary pressure is included. They used a graphical method for binary mixtures to check the state of equal chemical potentials and minimum Gibbs free energy. This method is illustrated in **Fig. 4** for the binary mixture C_1/C_6 at 130°F. Fig. 4a is a plot of the Gibbs free energy of oil at 600 psi and gas at 1,100 psi assuming oil is the wetting phase and gas is the reference phase. A tangent line has been drawn between the liquid curve and the gas curve. Mixtures with a composition between the tangent points will be unstable and split into gas and oil phases because the two-phase Gibbs free energy will be lower than the single-phase Gibbs free energy. The black dashed lines show the boundaries of the two-phase region. Equivalently, the state of equilibrium can also be depicted using plots of the chemical potentials for each component at each pressure (Fig. 4b). The horizontal line connecting Point A on the methane curve at 600 psi with Point B on the methane curve at 1,100 psi with the same chemical potentials for methane in each phase is a tie-line for all two-phase mixtures between Points A and B. Similarly, the tie-line for *n*-hexane connects Point C at 600 psi with Point D at 1,100 psi. Points A and C must line up vertically so the mole fractions in the liquid phase add to unity and Points B and D must line up vertically so the mole fractions in the gas phase add to unity.

New Criterion for Selection of the EOS Roots. When solved for compressibility factor, cubic EOSs can have either one or three real roots for each phase at a given fluid composition, temperature, and pressure. For the case of three real roots, the usual procedure is to select the root with the lowest Gibbs free energy for each specific phase. However, separately minimizing the Gibbs free energy of each phase does not guarantee a minimum in the total Gibbs free energy. This concern was raised previously (Whitson and Brule 2000), but no specific example of a failure of the conventional approach was presented, nor have we been able to find an example in the literature. In this subsection, we provide an example and then introduce a new stability criterion to solve this problem.

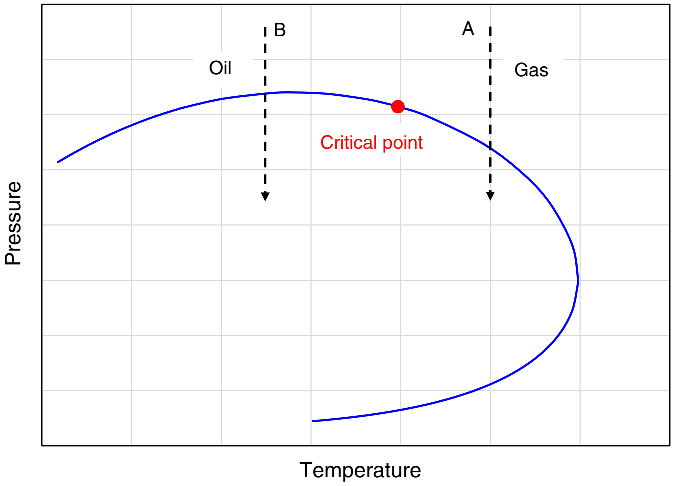

Fig. 3—Selection of the reference phase depending on phase continuity and initial state. Process A starts at single-phase gas state and Process B starts at single-phase liquid state. The critical point is indicated by red marker. The diagram is not to scale.

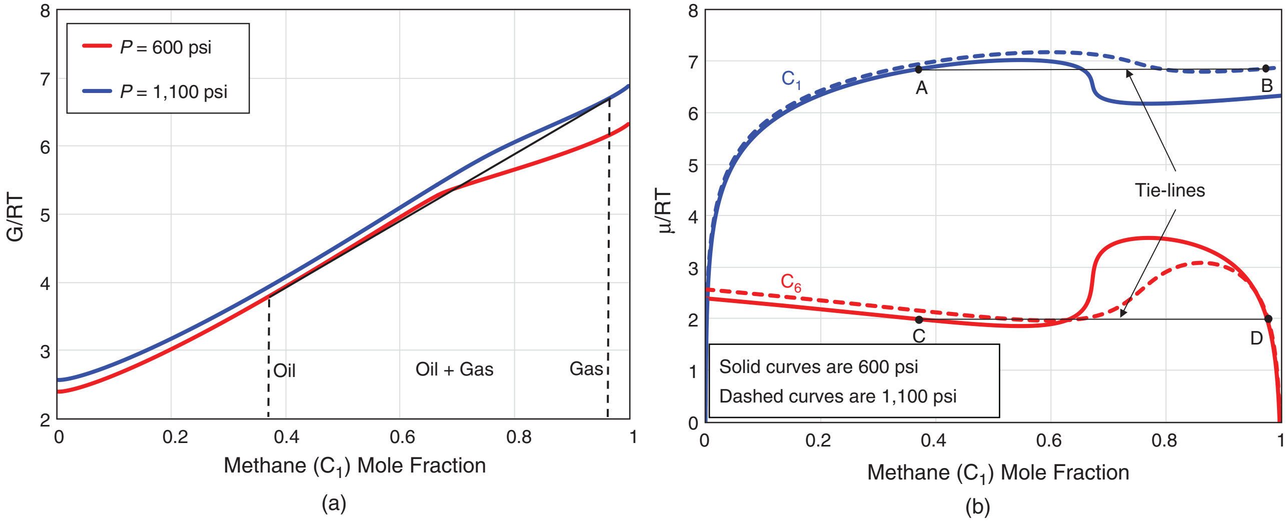

(a)

(b)

Fig. 4—(a) Plots of dimensionless Gibbs free energy (G/RT) for wetting- and nonwetting-phase pressures of 600 and 1,100 psi, respectively; the common tangent line (black line) represents the existence of a solution with minimum Gibbs free energy. The black dashed lines show the phase boundaries of the mixture. (b) Chemical potentials for C_1 and C_6 at 600 and 1,100 psi and the corresponding tie-lines; Points A and C show the mole fraction of C_1 in oil and Points B and D show the mole fraction of C_1 in gas.

Fig. 5a shows the Gibbs free energies calculated for C_1 and C_6 at 130°F and two pressures, 100 and 1,100 psi. In this example, the PR EOS provides three real roots between methane mole fractions of 0.07 and 0.58. The kink on the curve of Gibbs free energy at 100 psi and a mole fraction of 0.4 is caused by changing of the EOS roots to minimize local energy of this hypothetical single phase. As shown in Fig. 5a, no common tangent line can be constructed between the curves of Gibbs free energy at 100 and 1,100 psi. This is equivalent to the condition of inconsistent tie-lines that do not line up for both components for oil at 100 psi and gas at 1,100 psi (Fig. 5b). Therefore, the conventional approach of separately minimizing Gibbs free energies of each phase provides no two-phase solution at a capillary pressure of 1,000 psi. For an overall methane concentration of 0.7, Point Q in Fig. 5a shows the Gibbs free energy of the assumed single-phase mixture. Rezaveisi et al. (2015) reported that switching from a two-phase to a single-phase solution can lead to a phase discontinuity that not only is physically incorrect, but also causes limitations when simulating tight reservoirs with high capillary pressures in very small pores.

In **Fig. 6a,** the Gibbs free energy at 100 psi is calculated without changing the cubic EOS root between the mole fractions of 0.4 and 0.58. At 100 psi and a methane mole fraction of 0.48, the three real roots of the EOS in terms of compressibility factors are $Z_1 = 0.0295$, $Z_2 = 0.0814$, and $Z_3 = 0.8714$. Z_2 corresponds to a thermodynamically unstable solution and must be rejected. The largest root, Z_3, provides the lowest Gibbs free energy for the phase at 100 psi, but no two-phase solution can be found, as shown in Fig. 5. The smallest root, Z_1, results in a higher Gibbs free energy for the phase at 100 psi, but as shown in Fig. 6a, a common tangent line can now be constructed from the Gibbs-free-energy curve at 100 psi to the curve at 1,100 psi. For any composition between the tangent points, the mixture splits into two phases with a total Gibbs free energy less than the Gibbs free energy of a single phase at 1,100 psi. For example, the two-phase Gibbs free energy (G/RT) of 5.32 at Point Q' is lower than the single-phase G/RT of 5.61 at Point Q. Rezaveisi et al. (2015) studied the same mixture and did not find a solution at this capillary pressure, whereas a solution was found with the new approach. The equilibrium state can also be interpreted by plots of chemical potentials. Fig. 6b shows tie-lines calculated using the new criterion for selection of EOS roots. The oil phase is at its spinodal boundary at this capillary pressure. For higher capillary pressures, no two-phase solution can be found. Using the new root selection criterion to enforce the minimization of the total Gibbs free energy results in finding new solutions to the problem of capillary equilibrium at high capillary pressures. For a C_1-C_6 mixture at a capillary pressure of 1,000 psi, the oil/gas IFT is 0.228 dyne/cm. The pore diameter corresponding to this IFT is on the order of 0.2 nm.

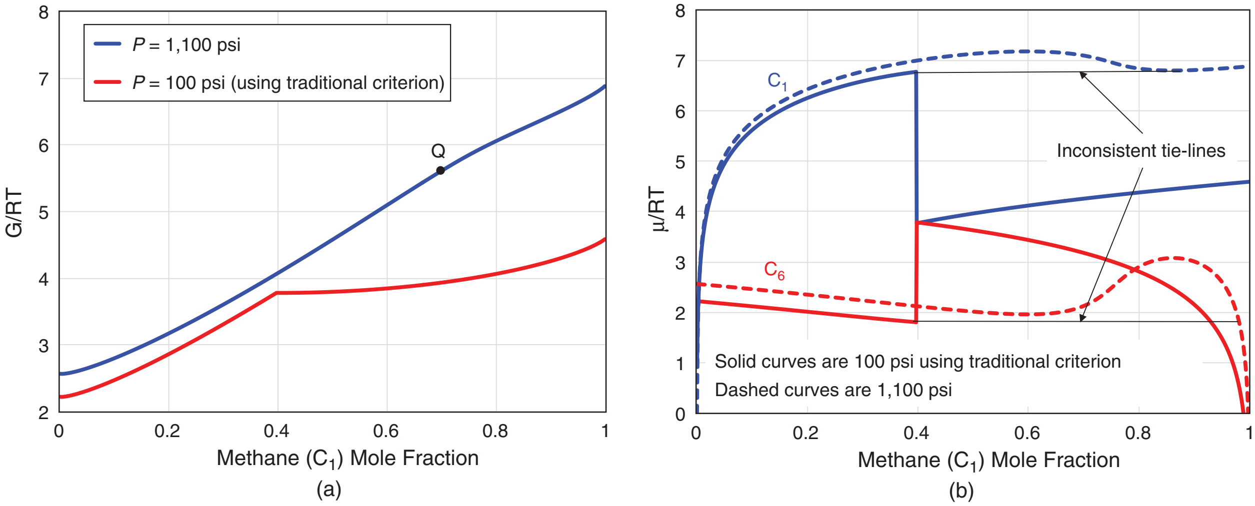

Fig. 5—(a) No common tangent line to the Gibbs-free-energy curves for hypothetical single-phase mixtures at 1,100 and 100 psi can be found using the conventional EOS root-selection method. (b) The tie-lines drawn between C_1 and C_6 chemical potentials at 1,100 and 100 psi do not line up, so a two-phase solution does not exist.

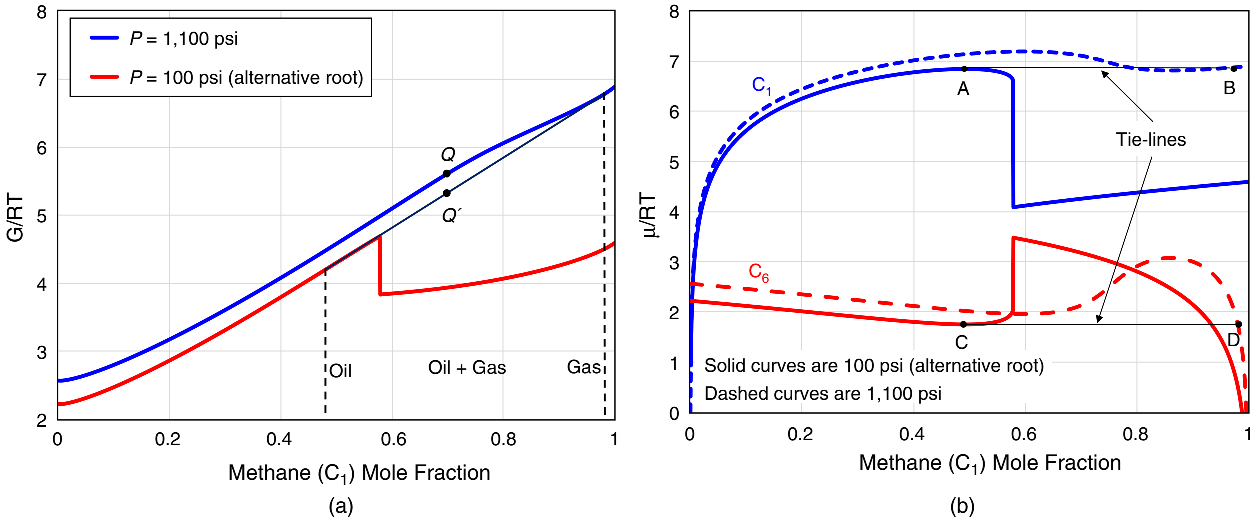

Fig. 6—(a) A common tangent line to the Gibbs-free-energy curves exists when using the new EOS root-selection method. The black vertical dashed lines show the phase boundaries of the mixture. (b) Chemical potentials at 1,100 psi (dashed curves) and 100 psi (solid lines) using the new criterion for selection of the cubic EOS roots; the tie-lines line up, so a two-phase solution exists. Points A and C show the mole fraction of C_1 in oil, and Points B and D show the mole fraction of C_1 in gas.

Uncertainty in Thermodynamic Models. There are uncertainties in both the models and parameters used to make the thermodynamic calculations, including capillary pressure. Identification of these uncertainties and their effects on the calculations is important and should be considered when the results are interpreted. All the calculations are affected by the choice of the EOS (e.g., PR EOS or SRK EOS).

Both the PR and SRK EOSs can underestimate liquid-phase density (Péneloux et al. 1982; Jhaveri and Youngren 1988). A correction factor known as the VSP can be used to improve the accuracy of the liquid-density calculation:

$$\tilde{V}_o = V_o - c. \qquad (4)$$

The corrected oil molar volume is then used to modify oil density and saturation. The change in oil saturation affects the capillary pressure (Eq. 1), which itself affects the equilibrium state. BICs and acentric factors are also uncertain and affect the EOS calculations.

We used the Macleod equation to calculate IFT:

$$\sigma_{og} = \left[\sum_{i=1}^{n_c} \chi_i (x_i \rho_o - y_i \rho_g)\right]^E . \quad (5)$$

Several authors have proposed different values for the scaling exponent (E) in Eq. 5. These values range from $E = 3.66$ (Hough and Stegemeier 1961) to $E = 4.0$ (Weinaug and Katz 1943). Schechter and Guo (1998) analyzed experimental data for various components occurring in reservoir fluids and found that $E = 3.88$ is a valid scaling exponent for pure components. Use of different exponents provides different values for IFT, and thus capillary pressures and phase behavior.

Effect of Capillary Pressure on Phase Behavior

The petrophysical and thermodynamic models discussed previously were used to evaluate the effect of capillary pressure on the phase behavior of hydrocarbon mixtures. All calculations were performed using the PR EOS with VSP correction, an IFT scaling exponent of $E = 3.88$, and the pore-size distribution measured for Sample 2 (Fig. 2). The measured porosity, permeability, and pore-radius mode of this sample are 7%, 4 µd, and 20 nm (Xu and Torres-Verdin 2014).

Estimation of Bubblepoint and Dewpoint Pressures. High capillary pressure changes the boundary of the two-phase region. Experimental measurements show that the bubblepoint pressure is suppressed, whereas the dewpoint pressure is increased (Trebin and Zadora 1968; Luo et al. 2016). The effect of pore-size distribution affects the capillary pressure and thus the phase behavior.

Fig. 7 shows the shift in phase envelopes of different binary mixtures using an STM ($r = 20$ nm) and the saturation-dependent function given in Eq. 1 for capillary pressure. The EOS parameters for this binary mixture are presented in **Table 1.** For temperatures lower than critical values, the bubblepoint pressure is suppressed by capillary pressure. The appearance of gas bubbles in larger pores corresponds to very high saturation of wetting phase and thus lower capillary pressure, according to Eq. 1. However, this fact is neglected when an STM with an average pore radius is used, and thus the suppression in bubblepoint is overestimated. The IFT and thus capillary pressure approach zero as the critical point is approached, so bubblepoint suppression also approaches zero. On the right-hand side of the critical point, the upper dewpoint increases. The appearance of the liquid phase in the smallest pores corresponds to very high nonwetting-phase saturations and thus very high capillary pressures. The IFT is lower near the upper dewpoint than near the lower dewpoint, so the lower dewpoint is more affected by capillary pressure than the upper dewpoint. The cricondentherm also shifts toward a higher pressure, and the two-phase region is expanded. The STM fails to predict such behavior and underestimates the shifts in both upper- and lower-dewpoint curves.

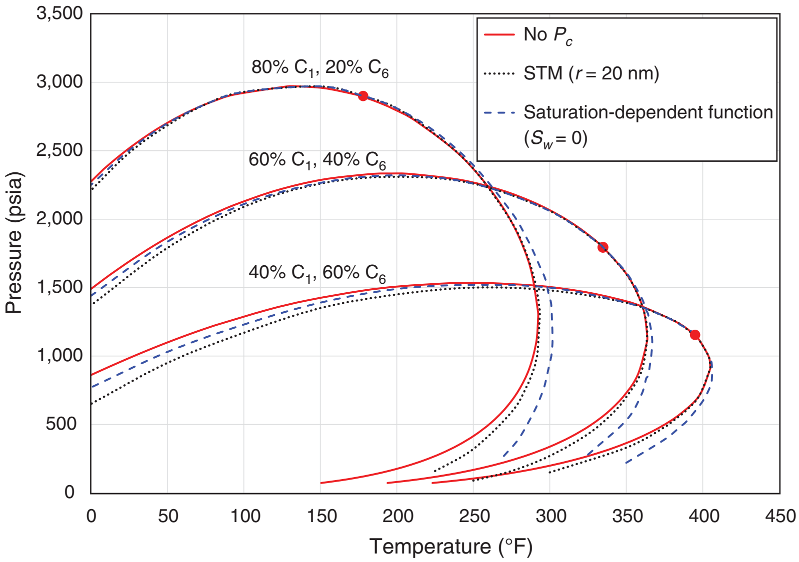

Fig. 7—Effect of capillary pressure on bubblepoint and dewpoint pressures of three different mixtures assuming no capillary pressure (red solid lines), STM with $r = 20$ nm (black dotted lines), and capillary pressure model tuned for Sample 2 with pore-size distribution (blue dashed lines). The STM overestimates the suppression of the bubblepoint and underestimates the change in the dewpoint curve.

	Molecular Weight (lbm/lbm mol)	Critical Pressure (psia)	Critical Temperature (°R)	Parachor	Acentric Factor	PR VSP (ft^3/lbm mol)	SRK VSP (ft^3/lbm mol)
C_1	16.04	667.2	343.08	77.3	0.008	–0.08	0.01
C_6	86.16	430.6	913.32	271.0	0.296	0.02	0.29

Table 1—EOS parameters for the binary mixtures of C_1 and C_6. The BIC used is zero.

The effect of connate water must also be included when the effect of capillary pressure on bubblepoint and dewpoint pressures of reservoir fluids in unconventional plays is investigated. This analysis was performed using the reported rock and fluid properties of a Middle Bakken tight oil reservoir (Yu et al. 2015). The PR EOS parameters and BICs are presented in **Tables 2 and 3.** The porosity, permeability, and initial water saturation of the formation are 6%, 5 µd, and 41%, respectively. The average pore radius can be roughly estimated as 25 nm using

$$r_{\text{ave}} = \sqrt{\frac{8k}{\phi}}. \qquad (6)$$

	Mole Fraction	Molecular Weight (lbm/lbm mol)	Critical Pressure (psia)	Critical Temperature (°R)	Parachor	Acentric Factor	PR VSP (ft^3/lbm mol)
CO_2	0.0002	44.01	1,069.86	547.56	78.0	0.225	–0.03
N_2	0.0004	28.01	492.31	227.16	41.0	0.040	–0.07
C_1	0.25	16.04	667.19	343.08	77.0	0.008	–0.08
$C_{2–4}$	0.22	42.82	625.16	653.94	145.2	0.143	–0.1
$C_{5–7}$	0.20	83.74	496.13	920.81	250.0	0.247	0.02
$C_{8–9}$	0.13	105.91	454.25	1,042.81	306.0	0.286	0.11
C_{10+}	0.1994	200.00	317.14	1,419.73	686.3	0.687	0.74

Table 2—PR EOS parameters for Middle Bakken oil.

	CO_2	N_2	C_1	$C_{2–4}$	$C_{5–7}$	$C_{8–9}$	C_{10+}
CO_2	0	–	–	–	–	–	–
N_2	–0.020	0	–	–	–	–	–
C_1	0.103	0.03	0	–	–	–	–
$C_{2–4}$	0.133	0.08	0.008	0	–	–	–
$C_{5–7}$	0.141	0.111	0.024	0.0046	0	–	–
$C_{8–9}$	0.150	0.120	0.032	0.0087	0.001	0	–
C_{10+}	0.150	0.120	0.078	0.0384	0.017	0.011	0

Table 3—PR EOS BICs used for Middle Bakken oil.

Furthermore, the mode of the pore-radius distribution in this formation is reported as 19 nm (Nojabaei et al. 2013). These values are very close to the measured values for Sample 2 in Fig. 2, so we use its corresponding capillary pressure function for the Middle Bakken tight oil reservoir. **Fig. 8** shows the shift in phase envelope at different connate-water saturations. For this water-wet reservoir, the effect of connate water on bubblepoint is not very significant because water occupies the smaller pores, whereas gas forms in larger pores. However, using a saturation-dependent capillary pressure function that accounts for pore-size distribution and 41% connate water is more accurate than an STM.

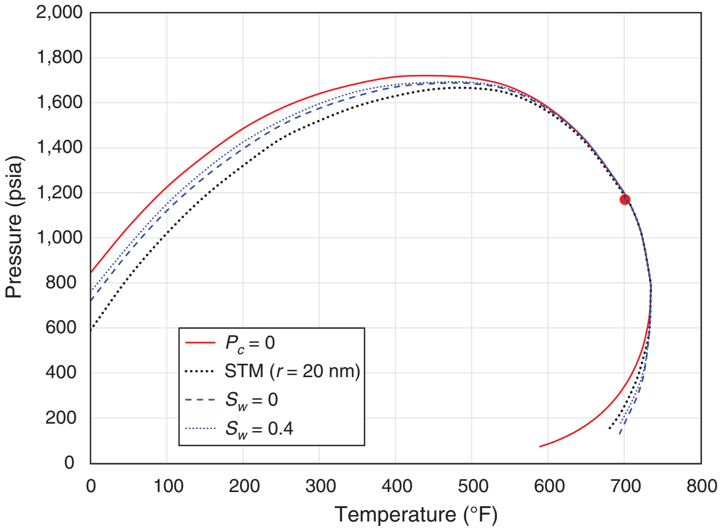

Fig. 8—Effect of capillary pressure on Middle Bakken tight oil formation using STM ($r = 20$ nm) and saturation-dependent model (Eq. 1) at different connate-water saturations.

CME Calculations. CME is used to measure the phase behavior for a fixed temperature and composition. In this method, the mixture is initially a single phase. The pressure is then decreased by increasing the volume in successive steps, and the volumes of the gas and liquid phases are measured. **Fig. 9a** shows the calculated gas saturation during CME for two binary mixtures at several connate-water saturations. The mixture of 40% C_1 and 60% C_6 at 130°F is initially 100% oil. At less than the bubblepoint, the gas saturation continuously increases as pressure decreases. Including capillary pressure results in forming more liquid and lowering the gas saturations. Connate water reduces the effect of capillary pressure. Fig. 9b shows the oil saturation during CME at 225°F for a binary mixture of 80% C_1 and 20% C_6. The mixture is initially 100% gas. As pressure decreases to less than the upper dewpoint, the oil saturation increases and then undergoes a retrograde behavior until decreasing to zero again at a lower pressure. The effect of capillary pressure and connate water on oil saturation is shown in Fig. 9b.

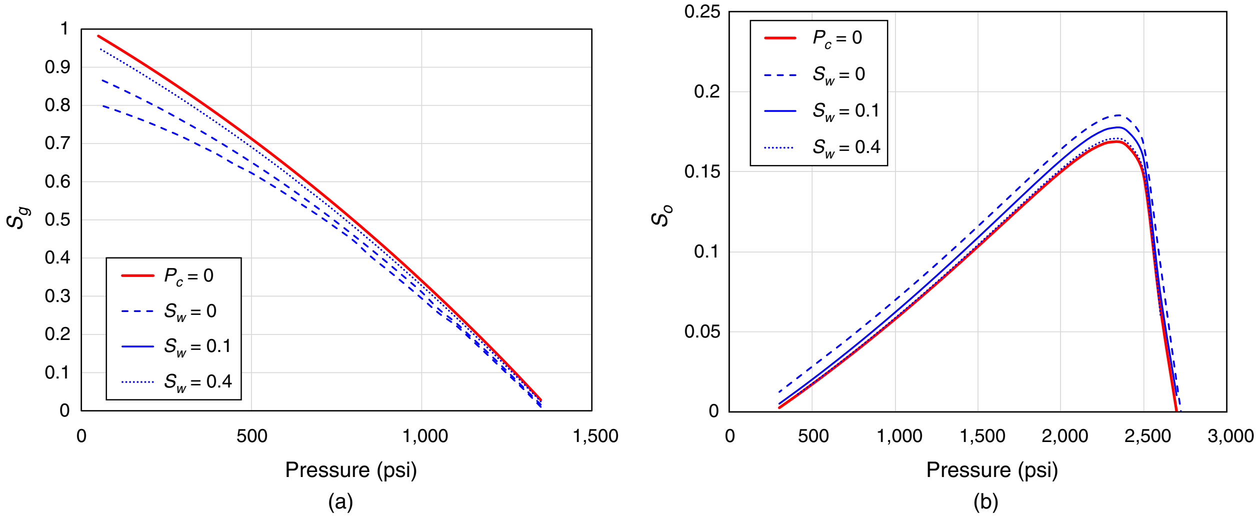

Fig. 9—Effect of capillary pressure on CME calculations. (a) Gas saturation for binary mixture of 40% C_1 and 60% C_6 at 130°F. (b) Liquid saturation for binary mixture of 80% C_1 and 20% C_6 at 225°F.

The term $\sqrt{\frac{\phi}{k}}$ in Eq. 1 scales the capillary pressure with permeability and porosity. The mode of the pore-diameter distribution for Sample 2 is 40 nm. This implies that $\sqrt{\frac{\phi}{k}}$ is two times higher when the median pore diameter is 10 nm. In **Fig. 10,** the CME calculations for the two binary mixtures are repeated using twice the value for $\sqrt{\frac{\phi}{k}}$. Capillary pressure is more influential in these cases. **Fig. 11** shows the CME calculations for the Middle Bakken tight oil formation. In this example, using a saturation-dependent capillary pressure function including the effect of connate water makes a significant improvement in the results compared with an STM.

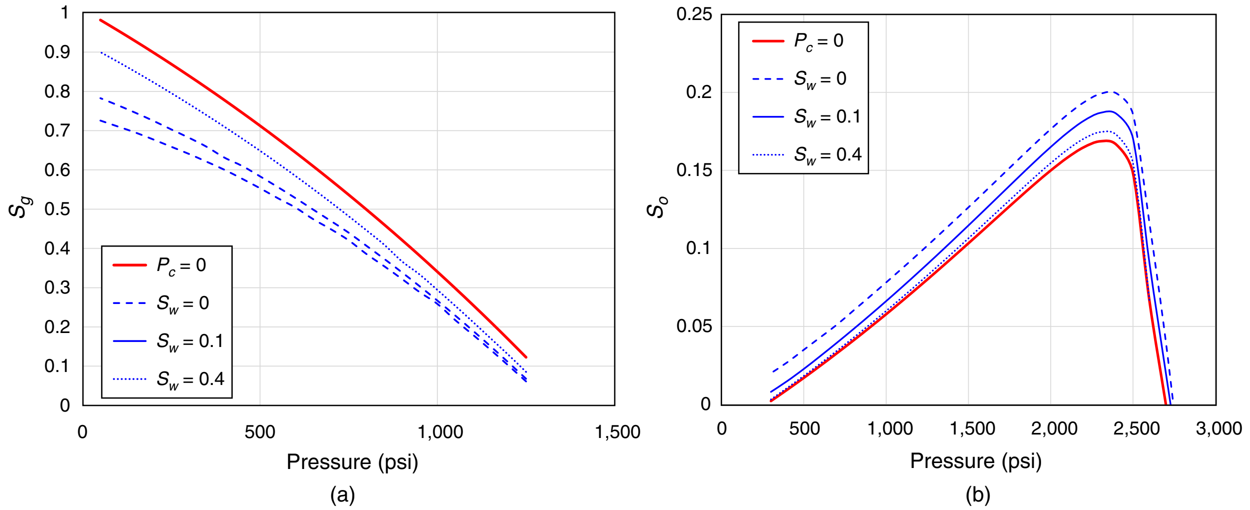

Fig. 10—Effect of capillary pressure on CME calculations using twice the value for $\sqrt{\frac{\phi}{k}}$. (a) Gas saturation for the binary mixture of 40% C_1 and 60% C_6 at 130°F. (b) Liquid saturations for the binary mixture of 80% C_1 and 20% C_6 at 225°F.

Fig. 12 shows the CME results using the gas/condensate composition reported for the Eagle Ford Shale Formation (Orangi et al. 2011). The PR EOS parameters and BICs are presented in **Tables 4 and 5.** The porosity, permeability, and initial water saturation of the formation are 9%, 0.5 μd, and 20 to 40%, respectively. Using Eq. 6, the average pore radius for this formation is approximately 7 nm, and thus the capillary pressure values measured for Sample 2 were multiplied by 2.8 to achieve an appropriate estimation for this case. The results indicate the importance of including the effect of connate-water saturation in the calculations.

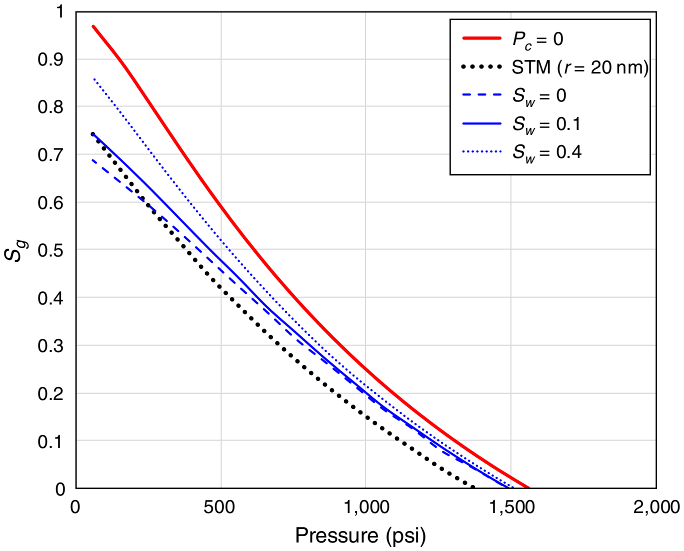

Fig. 11—CME calculations for Middle Bakken tight oil formation at 240°F. The saturation-dependent capillary pressure function including connate-water effect provides a much-better prediction compared with STM.

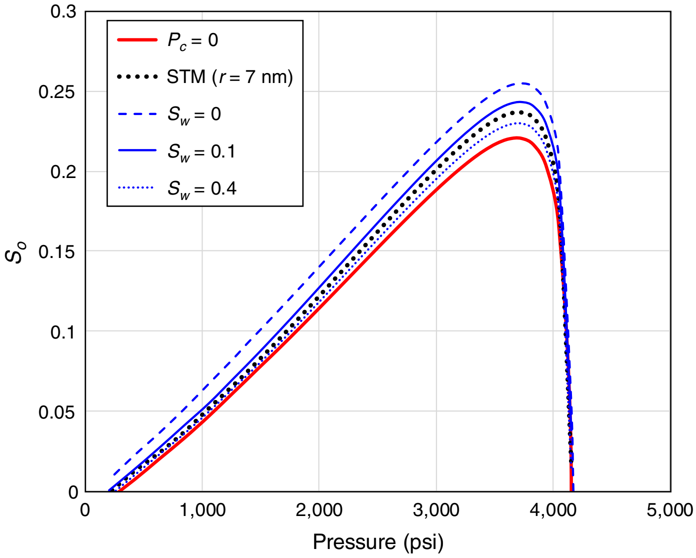

Fig. 12—CME calculations for Eagle Ford Shale gas/condensate reservoir at 200°F. The saturation-dependent capillary pressure function including connate-water effect provides a much-better prediction compared with STM.

	Mole Fraction	Molecular Weight (lbm/lbm mol)	Critical Pressure (psia)	Critical Temperature (°R)	Parachor	Acentric Factor	PR VSP (ft^3/lbm mol)
C_1	0.7075	16.04	673.08	343.26	77.3	0.013	–0.154
N_2	0.0017	28.01	492.32	227.16	41.0	0.040	–0.166
C_2	0.0894	30.07	708.35	549.77	108.9	0.097	–0.100
C_3	0.0498	44.10	617.38	665.82	151.9	0.152	–0.085
CO_2	0.0289	44.01	1071.3	547.56	78.0	0.225	–0.062
i-C_4	0.0110	58.12	529.06	734.91	181.5	0.185	–0.079
n-C_4	0.0190	58.12	550.66	765.69	191.7	0.201	–0.064
i-C_5	0.0081	72.15	483.50	829.05	225.0	0.222	–0.044
n-C_5	0.0073	72.15	489.52	845.61	233.9	0.254	–0.042
n-C_6	0.0067	86.18	439.70	913.65	271.0	0.300	–0.015
$C_{7–10}$	0.0428	112.00	408.59	1051	311.0	0.367	–0.015
$C_{11–14}$	0.0256	175.00	296.89	1,245.9	471.0	0.549	0.101
$C_{15–19}$	0.0016	210.00	259.01	1,327.6	556.3	0.643	0.134
C_{20+}	0.0008	250.00	226.28	1,405.8	836.4	0.753	0.164

Table 4—PR EOS parameters for Eagle Ford gas/condensate.

	C_1	N_2	C_2	C_3	CO_2	i-C_4	n-C_4	i-C_5	n-C_5	n-C_6	$C_{7–10}$	$C_{11–14}$	$C_{15–19}$	C_{20+}
C_1	0	–	–	–	–	–	–	–	–	–	–	–	–	–
N_2	0.036	0	–	–	–	–	–	–	–	–	–	–	–	–
C_2	0	0.05	0	–	–	–	–	–	–	–	–	–	–	–
C_3	0	0.08	0	0	–	–	–	–	–	–	–	–	–	–
CO_2	0.1	–0.02	0.13	0.135	0	–	–	–	–	–	–	–	–	–
i-C_4	0	0.095	0	0	0.13	0	–	–	–	–	–	–	–	–
n-C_4	0	0.09	0	0	0.13	0	0	–	–	–	–	–	–	–
i-C_5	0	0.095	0	0	0.125	0	0	0	–	–	–	–	–	–
n-C_5	0	0.1	0	0	0.125	0	0	0	0	–	–	–	–	–
n-C_6	0	0.1	0	0	0.125	0	0	0	0	0	–	–	–	–
$C_{7–10}$	0.024	0.148	0.019	0.014	0.111	0.010	0.005	0.005	0.005	0	0	–	–	–
$C_{11–14}$	0.051	0.202	0.041	0.031	0.095	0.020	0.010	0.01	0.010	0	0	0	–	–
$C_{15–19}$	0.062	0.223	0.049	0.037	0.089	0.025	0.012	0.012	0.012	0	0	0	0	–
C_{20+}	0.074	0.247	0.059	0.044	0.082	0.029	0.015	0.015	0.015	0	0	0	0	0

Table 5—PR EOS BICs used for Eagle Ford gas/condensate.

Sensitivity of the Results to the Uncertainties. An important part of our analysis is to evaluate the effect of uncertainties in the models and model parameters on the phase behavior. **Fig. 13** shows the results of CME calculations for the C_1/C_6 mixture at 130°F for different EOSs and VSPs. The results show that the calculations using the SRK EOS are more sensitive to VSP than those using the PR EOS for this particular case. The VSP affects the phase-behavior calculations with capillary pressure in two ways: one through phase saturations and the other through the IFT correlation, both of which affect capillary pressure. However, the sensitivity to VSP is low compared with the effect of capillary pressure. For this binary mixture at this temperature, changing the IFT scaling exponent from $E = 3.88$ to $E = 4$ does not have a significant effect on the calculations.

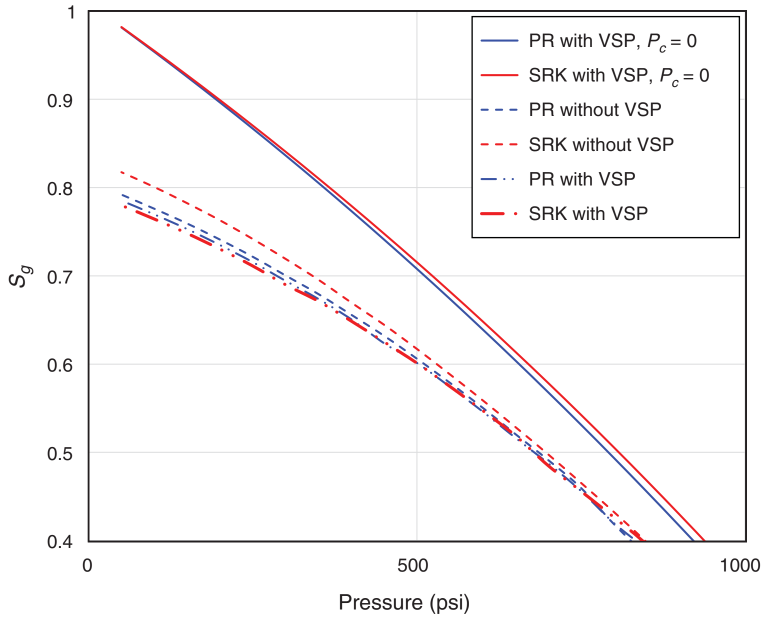

Fig. 13—Sensitivity of CME calculations to the choice of EOS (PR or SRK) and VSP for a binary mixture of 40% C_1 and 60% C_6 at 130°F.

CVD Calculations. Another common pressure/volume/temperature fluid analysis is CVD. CVD calculations were performed for binary mixtures consisting of 40% C_1 and 60% C_6 at 130°F and 80% C_1 and 20% C_6 at 225°F, as shown in **Fig. 14.** The CVD results for the Middle Bakken tight oil and Eagle Ford Shale gas/condensate formations are also shown in **Figs. 15 and 16.**

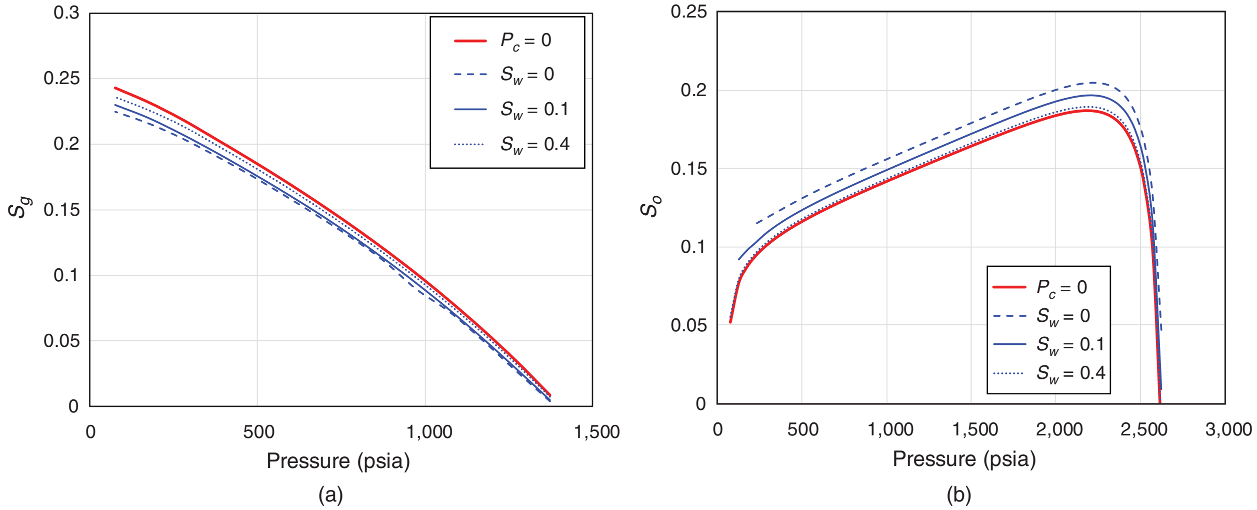

(a)

(b)

Fig. 14—CVD calculations including capillary pressure effect. (a) Gas saturation for a binary mixture of 40% C_1 and 60% C_6 at 130°F. (b) Liquid saturation for a binary mixture of 80% C_1 and 20% C_6 at 225°F.

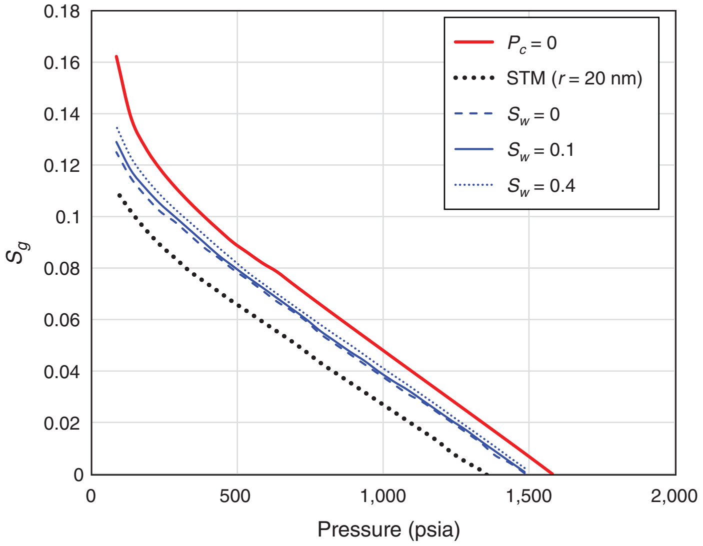

Fig. 15—CVD calculations for Middle Bakken tight oil formation at 240°F. The saturation-dependent capillary pressure function including connate-water effect provides a much-better prediction compared with the STM.

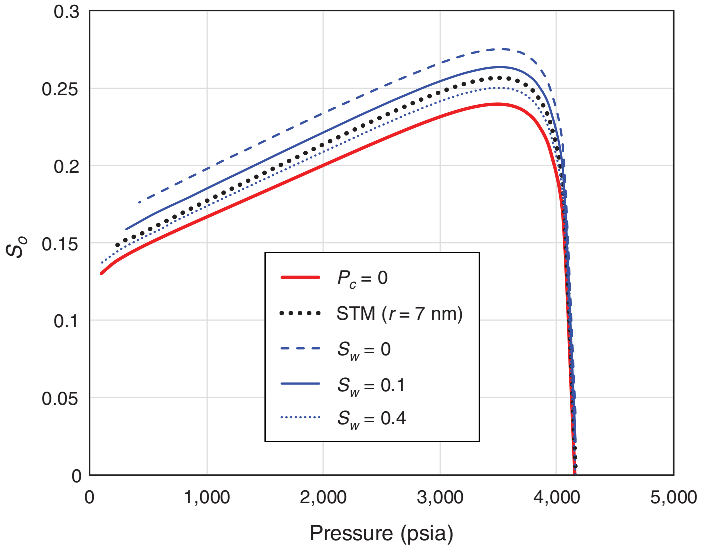

Fig. 16—CVD calculations for Eagle Ford Shale gas/condensate reservoir at 200°F. The saturation-dependent capillary pressure function including connate-water effect provides a much-better prediction compared with the STM.

Conclusions

A novel approach to estimating the effect of capillary pressure on the phase behavior in unconventional tight oil and shale-gas formations has been developed. The new method, for the first time, couples a rigorous thermodynamic analysis with several relevant petrophysical properties, such as pore-size distribution and connate-water saturation. First, a general three-phase capillary pressure model was introduced to estimate oil/gas capillary pressure in the presence of connate water. The new function was calibrated with measured capillary pressure data from unconventional formations with different pore-size distributions. A rigorous method for analysis of phase stability with capillary pressure was presented using plots of Gibbs free energy and chemical potential, and a new criterion for the selection of the cubic EOS roots was introduced. This new EOS root-selection criterion enabled us to find solutions without discontinuities at a capillary pressure as high as 1,000 psi. It was shown that the conventional method of selecting the cubic EOS roots fails to find these solutions. The new three-phase capillary pressure model and stability-analysis approach were used to investigate the phase behavior of binary and multicomponent reservoir fluids for Middle Bakken tight oil and Eagle Ford Shale gas/condensate formations. The prediction of bubblepoint and dewpoint pressures is significantly improved compared with an STM. The effect of capillary pressure, connate-water saturation, and pore-size distribution on CME and CVD calculations was illustrated. In particular, connate-water saturation can have a significant effect on phase behavior through its effect on capillary pressure even when the water solubility in the hydrocarbon phases is neglected. The sensitivity of these calculations to the EOS parameters was small compared with the effect of capillary pressure itself for the cases studied.

Nomenclature

a_g = capillary pressure exponent of gas
a_o = capillary pressure exponent of oil
b_g = capillary entry pressure of gas, m/Lt^2, psi
b_o = capillary entry pressure of oil, m/Lt^2, psi
c = VSP, L^3/N, ft^3/lbmol
E = IFT correlation exponent
k = permeability, L^2, md
$P_{c,og}$ = capillary pressure between oil and gas, m/Lt^2, psi
P_g = gas pressure, m/Lt^2, psi
P_o = oil pressure, m/Lt^2, psi
r_{ave} = average pore size in a porous medium, L, ft
R = gas constant, ML^2/t^{2}NT, psia-ft^3/lbmol-°R
S_g = gas saturation
S_o = oil saturation
S_{wc} = connate-water saturation
T = temperature, T, °F
V_o = oil molar volume, L^3/N, ft^3/lbmol
$\tilde{V}_o$ = oil molar volume corrected by VSP, L^3/N, ft^3/lbmol
x_i = mole fraction of component i in oil
y_i = mole fraction of component i in gas
μ_{ig} = chemical potential of component i in gas, mL^2/t^{2}N, Btu/lbmol
μ_{io} = chemical potential of component i in oil, mL^2/t^{2}N, Btu/lbmol
ρ_g = gas molar density, L^3/N, ft^3/lbmol
ρ_o = oil molar density, L^3/N, ft^3/lbmol
σ_{og} = oil/gas IFT, m/T^2, dyne/cm
ϕ = porosity
ϕ_{og} = contact angle for oil and gas
χ_i = parachor of component i

References

Al Hinai, A., Rezaee, R., Esteban, L. et al. 2014. Comparisons of Pore Size Distribution: A Case From the Western Australian Gas Shale Formations. *J. Unconven. Oil Gas Resour.* **159** (December): 1–13. https://doi.org/10.1016/j.juogr.2014.06.002.

Barsotti, E., Tan, S. P., Saraji, S. et al. 2016. A Review on Capillary Condensation in Nanoporous Media: Implications for Hydrocarbon Recovery from Tight Reservoirs. *Fuel* **184** (15): 344–361. https://doi.org/10.1016/j.fuel.2016.06.123.

Bradford, S. and Leij, F. 1995. Wettability Effects on Scaling Two- and Three-Fluid Capillary Pressure-Saturation Relations. *Environ. Sci. Technol.* **29** (6): 1446–1455. https://doi.org/10.1021/es00006a004.

Brusilovsky, A. I. 1992. Mathematical Simulation of Phase Behavior of Natural Multicomponent Systems at High Pressure With an Equation of State. *SPE Res Eng* **7** (1): 117–122. SPE-20180-PA. https://doi.org/10.2118/20180-PA.

Campos, M. D., Akkulu, I. Y., and Sigal, R. F. 2009. Molecular Dynamics Study on Natural Gas Solubility Enhancement in Water Confined to Small Pores. Presented at the SPE Annual Technical Conference and Exhibition, New Orleans, 4–7 October. SPE-124491-MS. https://doi.org/10.2118/124491-MS.

Clarkson, C. R., Solano, N., Bustin, R. M. et al. 2013. Pore Structure Characterization of No North American Shale Gas Reservoirs Using USANS/SANS, Gas Adsorption, and Mercury Intrusion. *Fuel* **103** (January): 606–616. https://doi.org/10.1016/j.fuel.2012.06.119.

Dernaika, M., Al Jallad, O., Koronfol, S. et al. 2015. Petrophysical and Fluid Flow Properties of a Tight Carbonate Source Rock Using Digital Rock Physics. Presented at the Unconventional Resources and Technology Conference, San Antonio, Texas, 20–22 July. URTEC-2154815-MS. https://doi.org/10.15530/URTEC-2015-2154815.

Hough, E. W. and Stegemeier, G. L. 1961. Correlation of Surface and Interfacial Tension of Light Hydrocarbons in the Critical Region. *SPE J.* **1** (4): 259–263. SPE-197-PA. https://doi.org/10.2118/197-PA.

Jhaveri, B. S. and Youngren, G. K. 1988. Three-Parameter Modification of the Peng-Robinson Equation of State To Improve Volumetric Predictions. *SPE J.* **3** (3): 1033–1040. SPE-13118-PA. https://doi.org/10.2118/13118-PA.

Kalaydjian, F.J-M. 1992. Performance and Analysis of Three-Phase Capillary Pressure Curves for Drainage and Imbibition in Porous Media. Presented at the SPE Annual Technical Conference and Exhibition, Washington, DC, 4–7 October. SPE-24878-MS. https://doi.org/10.2118/24878-MS.

Kuila, U. and Prasad, M. 2013. Specific Surface Area and Pore-Size Distribution in Clays and Shales. *Geophysical Prospecting* **61** (2): 341–362. https://doi.org/10.1111/1365-2478.12028.

Loucks, R. G., Reed, R. M., Ruppel, S. C. et al. 2009. Morphology, Genesis, and Distribution of Nanometer-Scale Pores in Siliceous Mudstones of the Mississippian Barnett Shale. *J. Sediment. Res.* **79** (12): 848–861. https://doi.org/10.2110/jsr.2009.092.

Luo, S., Nasrabadi, H., and Lutkenhaus, J. L. 2016. Effect of Confinement on the Bubble Points of Hydrocarbons in Nanoporous Media. *AlChE J.* **62** (5): 1772–1780. https://doi.org/10.1002/aic.15154.

Mehrabi, M., Javadpour, F., and Sepehrnoori, K. 2017. Analytical Analysis of Gas Diffusion into Non-Circular Pores of Shale Organic Matter. *J. Fluid Mech.* **819** (25 May): 656–677. https://doi.org/10.1017/jfm.2017.180.

Michelsen, M. 1982. The Isothermal Flash Problem. Part I. Stability. *Fluid Phase Equilibr.* **9** (1): 1–19. https://doi.org/10.1016/0378-3812(82)85001-2.

Nelson, P. 2009. Pore-Throat Sizes in Sandstones, Tight Sandstones, and Shales. *AAPG Bull.* **93** (3): 329–340. https://doi.org/10.1306/10240808059.

Neshat, S. S. and Pope. G. A. 2017. Compositional Three-Phase Relative Permeability and Capillary Pressure Models Using Gibbs Free Energy. Presented at the SPE Reservoir Simulation Conference, Montgomery, Texas, 20–22 February. SPE-182592-MS. https://doi.org/10.2118/182592-MS.

Newsham, K. E., Lasswell, P. M., Cox, J. C. et al. 2004. A Comparative Study of Laboratory Techniques for Measuring Capillary Pressures in Tight Gas Sands. Presented at the SPE Annual Technical Conference and Exhibition, Houston, 26–29 September. SPE-89866-MS. https://doi.org/10.2118/89866-MS.

Nojabaei, B., Johns, R. T., and Chu, L. 2013. Effect of Capillary Pressure on Phase Behavior in Tight Rocks and Shales. *SPE J.* **16** (3): 281–289. SPE-159258-PA. https://doi.org/10.2118/159258-PA.

Orangi, A., Nagarajan, N. R., Honarpour, M. M. et al. 2011. Unconventional Shale Oil and Gas-Condensate Reservoir Production, Impact of Rock, Fluid, and Hydraulic Fractures. Presented at the SPE Hydraulic Fracturing Technology Conference, The Woodlands, Texas, 24–26 January. SPE-140536-MS. https://doi.org/10.2118/140536-MS.

Peng, D. Y. and Robinson, D. B. 1976. A New Two-Constant Equation of State. *Ind. Eng. Chem. Fundamen.* **15** (1): 59–64. https://doi.org/10.1021/i160057a011.

Péneloux, A., Rauzy, E., and Fréze, R. 1982. A Consistent Correction for Redlich-Kwong-Soave Volumes. *Fluid Phase Equilibr.* **8** (1): 7–23. https://doi.org/10.1016/0378-3812(82)80002-2.

Rachford, J. H. and Rice, J. D. 1952. Procedure for Use of Electronic Digital Computers in Calculating Flash Vaporization Hydrocarbon Equilibrium. *J Pet Technol* **4** (10): 327–328. https://doi.org/10.2118/952327-G.

Rezaveisi, M., Sepehrnoori, K., Pope, G. A. et al. 2015. Compositional Simulation Including Effect of Capillary Pressure on Phase Behavior. Presented at the SPE Annual Technical Conference and Exhibition, Houston, 28–30 September. SPE-175135-MS. https://doi.org/10.2118/175135-MS.

Russo, P. A., Carrott, M. M. L. R., and Carrott, P. J. M. 2011. Hydrocarbons Adsorption on Templated Mesoporous Materials: Effect of the Pore Size, Geometry and Surface Chemistry. *New J. Chem.* **35** (2): 407–416. https://doi.org/10.1039/C0NJ00614A.

Sandoval, D., Yan, W., Michelsen, M. et al. 2016. The Phase Envelope of Multicomponent Mixtures in the Presence of a Capillary Pressure Difference. *Ind. Eng. Chem. Res.* **55** (22): 6530–6538. https://doi.org/10.1021/acs.iecr.6b00972.

Schechter, D. S. and Guo, B. 1998. Parachors Based on Modern Physics and Their Uses in IFT Prediction of Reservoir Fluids. *SPE J.* **1** (3): 207–217. SPE-30785-PA. https://doi.org/10.2118/30785-PA.

Shapiro, A. and Stenby, E. 2001. Thermodynamics of the Multicomponent Vapor-Liquid Equilibrium Under Capillary Pressure Difference. *Fluid Phase Equilibr.* **178** (1–2): 17–32. https://doi.org/10.1016/S0378-3812(00)00403-9.

Sigal, R. F. 2015. Pore-Size Distributions for Organic-Shale-Reservoir Rocks From Nuclear-Magnetic-Resonance Spectra Combined With Adsorption Measurements. *SPE J.* **20** (4): 824–830. SPE-174546-PA. https://doi.org/10.2118/174546-PA.

Sigmund, P. M., Dranchuk, P. M., Morrow, N. R. et al. 1973. Retrograde Condensate in Porous Media. *SPE J.* **13** (2): 93104. SPE-3476-PA. https://doi.org/10.2118/3476-PA.

Singh, S. K., Sinha, A., Deo, G. et al. 2009. Vapor-Liquid Phase Coexistence, Critical Properties, and Surface Tension of Confined Alkanes. *J. Phys. Chem. C* **113** (17): 7170–7180. https://doi.org/10.1021/jp8073915.

Soave, G. 1972. Equilibrium Constants From Modified Redlich-Kwong Equation of State. *Chem. Eng. Sci.* **27:** 1197–1203. https://doi.org/10.1016/0009-2509(72)80096-4.

Travalloni, L., Castier, M., Tavares, F. W. et al. 2010. Thermodynamic Modeling of Confined Fluids Using an Extension of the Generalized van der Waals Theory. *Chem. Eng. Sci.* **65** (10): 3088–3099. https://doi.org/10.1016/j.ces.2010.01.032.

Trebin, F. A. and Zadora, G. I. 1968. Experimental Study of the Effect of a Porous Media on Phase Changes in Gas Condensate Systems. *Neft'i Gaz* **8** (1): 37–40.

Virnovsky, G. A., Vatne, O. K., Iversen, J. E. et al. 2004. Three-Phase Capillary Pressure Measurements in Centrifuge at Reservoir Conditions. Presented at the International Symposium of the Society of Core Analysts, Abu Dhabi, 5–9 October. SCA 2004-19.

Wang, L., Yin, X., Neeves, K. B. et al. 2016. Effect of Pore-Size Distribution on Phase Transition of Hydrocarbon Mixtures in Nanoporous Media. *SPE J.* **21** (6): 1981–1995. SPE-170894-PA. https://doi.org/10.2118/170894-PA.

Weinaug, C. F. and Katz, D. L. 1943. Surface Tensions of Methane-Propane Mixtures. *Ind. Eng. Chem.* **35** (2): 239–246. https://doi.org/10.1021/ie50398a028.

Whitson, C. H. and Brule, M. R. 2000. *Phase Behavior*, Vol. 20. Richardson, Texas: Monograph Series, Society of Petroleum Engineers.

Xu, C. and Torres-Verdin, C. 2014. Petrophysical Rock Classification in the Cotton Valley Tight-Gas Sandstone Reservoir With a Clustering Pore-System Orthogonality. *Interpretation* **2** (1): 13–23. https://doi.org/10.1190/INT-2013-0063.1.

Yu, W., Lashgari, H. R., Wu, K. et al. 2015. CO_2 Injection for Enhanced Oil Recovery in Bakken Tight Oil Reservoirs. *Fuel* **159** (1 November): 354–363. https://doi.org/10.1016/j.fuel.2015.06.092.

Zhang, L., Lu, S., Xiao, D. et al. 2017. Characterization of Full Pore Size Distribution and its Significance to Macroscopic Physical Parameters in Tight Glutenites. *J. Nat. Gas Sci. Eng.* **38** (February): 434–449. https://doi.org/10.1016/j.jngse.2016.12.026.

Sajjad S. Neshat is a PhD degree candidate at the University of Texas at Austin. His research interests include thermodynamics and phase behavior of reservoir fluids, modeling multiphase flow in porous media, compositional reservoir simulations, and data analysis. Neshat holds two bachelor's degrees in petroleum engineering and mechanical engineering, both from Sharif University of Technology, Iran, and a master's degree in mechanical engineering from the University of Texas at Austin.

Ryosuke Okuno is an assistant professor in the Hildebrand Department of Petroleum and Geosystems and Engineering at the University of Texas at Austin. Before his current position, he served as an assistant professor of petroleum engineering at the University of Alberta from 2010 to 2015. Okuno also has 7 years of industrial experience as a reservoir engineer with Japan Petroleum Exploration Company Limited and is a registered professional engineer in Alberta, Canada. His research and teaching interests include enhanced oil recovery (EOR), heavy-oil recovery, unconventional resources, numerical reservoir simulation, thermodynamics, multiphase behavior, and applied mathematics. Okuno holds bachelor's and master's degrees in geosystem engineering from the University of Tokyo and a PhD degree in petroleum engineering from the University of Texas at Austin. He is a recipient of the 2012 SPE Petroleum Engineering Junior Faculty Research Initiation Award, is an associate editor for *SPE Journal,* and holds the Pioneer Corporation Faculty Fellowship in Petroleum Engineering at the University of Texas at Austin.

Gary A. Pope is a professor in the Hildebrand Department of Petroleum and Geosystems Engineering at the University of Texas at Austin, where he holds the Texaco Centennial Chair in Petroleum Engineering. His teaching and research are in the areas of EOR, reservoir engineering, natural-gas engineering, and reservoir simulation. Pope was elected to the National Academy of Engineering in 1999. He holds a bachelor's degree from Oklahoma State University and a PhD degree from Rice University, both in chemical engineering. Pope was awarded SPE Honorary Member status and SPE Distinguished Member status and has received the AIME Environmental Conservation Award, the SPE Distinguished Service Award, the Billy and Claude R. Hocott Distinguished Centennial Engineering Research Award, the SPE IOR Pioneer Award, the SPE/AIME Anthony F. Lucas Gold Medal, the SPE John Franklin Carll Award, the SPE Distinguished Achievement Award, and the SPE Reservoir Engineering Award.